Chemical Geology 290 (2011) 109–120

Contents lists available at SciVerse ScienceDirect

Chemical Geology

journal homepage: www.elsevier.com/locate/chemgeo

Research paper

Nanostructured calcite precipitated under hydrothermal conditions in the presence of organic and inorganic selenium

G. Montes-Hernandez [a,*], G. Sarret [b,*], R. Hellmann [b], N. Menguy [c], D. Testemale [d], L. Charlet [b], F. Renard [a,e]

[a] ISTerre, CNRS UMR and Joseph Fourier University, OSUG, BP 53, 38041 Grenoble Cedex 9, France
[b] Environmental Geochemistry group, Géochimie 4D, ISTerre, CNRS UMR, Joseph Fourier University, OSUG, BP 53, 38041 Grenoble Cedex 9, France
[c] IMPMC, UMR 7590 CNRS - Université Pierre et Marie Curie - IRD, 4 place Jussieu 75252 Paris cedex 05, France
[d] Institut Néel, Département MCMF, CNRS, 25 Avenue des Martyrs, 38042 Grenoble, France
[e] Physics of Geological Processes, University of Oslo, Norway

ARTICLE INFO

Article history:
Received 18 May 2011
Received in revised form 7 September 2011
Accepted 10 September 2011
Available online 17 September 2011

Editor: J. Fein

Keywords:
Nanostructured material
Hydrothermal conditions
Selenite
Seleno-L-cystine
Crystallographic incorporation into calcite
Selenium

ABSTRACT

Selenium is an important trace metalloid, whose global cycle is controlled by fluid–rock interactions in the Earth's upper crust, interactions with bio-molecules in soils and living systems, and atmospheric transport in ashes. The cycling of selenium is often intimately associated with carbonate phases, with Se being generally incorporated as an impurity in calcite crystals or adsorbed on carbonate nanoparticles. In order to better understand the interaction of aqueous selenium species with carbonates, we studied the precipitation of calcite under hydrothermal conditions (30–90 °C, 25–90 bar) in a CO_2–H_2O–$Ca(OH)_2$ medium in the presence of aqueous inorganic and organic selenium compounds. Aqueous carbonation reactions in the presence of selenium at elevated temperatures and pressures, relevant for long-term CO_2 sequestration in reservoirs and other natural geological systems, have until now not been investigated to the best of our knowledge. Electron microscopy (FESEM and TEM) and synchrotron X-ray absorption spectroscopy (XAS) were used in a complementary manner to investigate crystal size, structural order (crystallinity), morphology of crystal faces, crystal organization, and selenium speciation in the calcite samples. XAS data analysis showed clear evidence for the incorporation of selenite oxyanion (SeO_3^{2-}) into the calcite crystal structure. At low Se content (1.3 mg/g calcite), a single site was observed with Se surrounded by six Ca atoms, whereas additional sites, probably corresponding to surface sorption sites, were found with increasing Se content. XAS also showed that seleno-L-cystine (Secys) was chemically fragmented during carbonation, and the solid phase contained elemental and oxidized Se, in hexagonal or amorphous form depending on the experimental conditions, with a minor proportion of Se(IV). Moreover, FESEM and TEM measurements revealed a very complex effect of Secys on the particle size and aggregation/agglomeration process, leading to the following calcite morphologies: rhombohedra, elongated rhombohedra (*c*-axis elongation), scalenohedra, star-like and shell-like crystal aggregates, and irregular calcite polycrystals. The aggregates and irregular polycrystals, which we designate as nanostructured calcite material, were constituted of nanometer-sized calcite crystallites (<100 nm). The star and shell-like crystal aggregates, which were observed only in the presence of Secys, may be due to crystal growth in the presence of associated secondary organic compounds due to a simultaneous chemical fragmentation of Secys. Overall, the results from this study show that selenium (of biotic or abiotic origin) can be integrated into the crystallographic structure of calcite under hydrothermal conditions. This has relevance for geological processes in diverse environments, such as hydrothermal systems along mid-ocean ridges, or underground reservoirs associated with massive injection of CO_2 for long-term geological sequestration.

1. Introduction

The biotic and abiotic (i.e. inorganic) formation of carbonates plays a crucial role in the global carbon cycle. Moreover, carbonate minerals often sequester various trace elements (actinides and lanthanides), metalloids, and heavy metals, and thus control in part their global cycling (e.g. Paquette and Reeder, 1995; Stumm and Morgan, 1995; Sigg et al., 2000; Stipp et al., 2006; Stumpf et al., 2006; Heberling et al., 2008; Schmidt et al., 2008, 2009). Selenium is one of these elements that can be taken up by carbonate phases. In addition to carbonates, selenium also occurs in many diverse geological environments: magmas, sulfide deposits associated with hydrothermal systems, oil and gas reservoirs, coal beds, and clays in black shales (Fouquet et al.,

* Corresponding authors.
E-mail addresses: german.montes-hernandez@obs.ujf-grenoble.fr (G. Montes-Hernandez), geraldine.sarret@obs.ujf-grenoble.fr (G. Sarret).

0009-2541/$ – see front matter © 2011 Elsevier B.V. All rights reserved.
doi:10.1016/j.chemgeo.2011.09.007

1996; Martens and Suarez, 1997; Malisa, 2001; Wen and Qiu, 2002; Rouxel et al., 2004; Yudovich and Ketris, 2006; Orberger et al., 2007). Selenium is also often considered to be a contaminant in the environment, and can be present in soils, ground waters, and the atmosphere. The source of contamination may come from natural selenium-rich geological formations that are altered naturally or anthropogenically, or from fly-ash leachates generated from the combustion of coal in electric power plants. Moreover, Se is also a long-lived, mobile fission product present in nuclear wastes, and thus has the potential to migrate into the far-field geological environment.

One of the reasons for studying Se uptake by calcite is that selenium is a beneficial trace element in living organisms (dietary deficiency for humans occurs at intakes less than 40 μg/day); on the other hand, it is deleterious to health (i.e. toxic) at elevated concentrations (>400 μg/day intake for humans); see Aurelio et al. (2010) and Levander and Burk (2006). Therefore, understanding selenium's mobility and its global cycle are necessary for better predicting its effect on the environmental quality of natural soils, as well as surface and ground water systems.

Selenium most commonly occurs in four different oxidation states in natural geological environments, namely −2, 0, +4, and +6. It can easily form compounds with metals. About fifty naturally-occurring minerals containing selenium have been identified. Past studies have shown that the fate and transport of Se in contaminated sites are influenced by its chemical form and speciation (see, e.g., Montes-Hernandez et al., 2008a, 2008b; Fernandez-Martinez and Charlet, 2009; and references therein). Selenium can also exist in organic molecules. For example, selenocystine (containing two amine and two carboxylic acid groups) is an analog to selenocysteine amino acid present in most living systems. It is naturally synthesized by several plants and can accumulate in soils (Martens and Suarez, 1997).

Carbonate minerals can be formed in natural or artificial environments by three different mechanistic pathways and/or conditions (e.g., Montes-Hernandez et al., 2010): (1) aqueous nucleation growth in homogeneous or heterogeneous systems, e.g., chemical or biogenic formation of carbonates in lakes, oceans, CO_2 storage sites, natural caves; (2) gas–solid carbonation of alkaline minerals (fine particles) in the presence of adsorbed water (water humidity conditions, 0<water activity<1), e.g., carbonate formation in water-unsaturated soils, in terrestrial or extraterrestrial aerosols; (3) dry gas–solid carbonation of granular/porous materials (dry conditions, water activity ≈ 0), e.g., the industrial mineralization, recovery, or capture of CO_2 at high temperatures in the presence of alkaline oxides (CaO, MgO) or metastable nanoparticle alkaline silicates. A brief description concerning the aqueous mineralization of CO_2 or aqueous carbonate formation in natural and industrial systems is provided in the supporting information (see text SI-1).

The nucleation growth of calcite has been widely studied in homogeneous (solution–solution interactions) or heterogeneous (solid–solution interactions) systems at atmospheric pressure and at moderate temperatures (<70 °C). Typical studies have used classical macroscopic, microscopic, or atomistic models to explain nucleation and growth (see e.g., Seifritz, 1990; Dove and Hochella, 1993; Lackner et al., 1995; Stumm and Morgan, 1995; Paquette and Reeder, 1995; Jonasson et al., 1996; Gower and Tirell, 1998; Teng et al., 1998; Temman et al., 2000; Dousi et al., 2003; Pastero et al., 2003; Freij et al., 2004; Fujita et al., 2004; Chrissanthopoulos et al., 2005; Dalas et al., 2006; Lee and Reeder, 2006; Menadakis et al., 2007; Montes-Hernandez et al., 2007; Nehrke et al., 2007). The incorporation of various oxyanions (e.g., selenite, selenate, arsenite, arsenate) into calcite has also been investigated in homogeneous or heterogeneous systems (e.g. Paquette and Reeder, 1995; Cheng et al., 1997, 1999; Roman-Ross et al., 2006; Alexandratos et al., 2007). For example, Reeder et al. (1994) have shown that selenate (SeO_4^{2-}) oxyanion substitutes for carbonate anion (CO_3^{2-}) in calcite. Other tetrahedral oxyanions, including CrO_4^{2-} and AsO_4^{3-}, have been found to substitute for CO_3^{2-} in calcite (Alexandratos et al., 2007; Tang et al., 2007). In all of these studies, the Ca shell was fitted with two Ca sub-shells, suggesting that the metal(loïd) was off-centered compared to the position of the carbon atom from the carbonate group in pure calcite.

Several studies have demonstrated that the incorporation and/or sorption of inorganic/organic impurities inhibit the crystal growth process of calcite (e.g., Dove and Hochella, 1993; Paquette and Reeder, 1995; Freij et al., 2004; Dalas et al., 2006). Conversely, the nucleation process may be enhanced, leading to a complex aggregation/agglomeration process of small particles, resulting in clusters or crystallites, as observed in present study. When the dimensions of the clusters or crystallites are in the 1 to 100 nm range, the solid is commonly termed a nanostructured material. While the effects of inorganic/organic aqueous selenium on calcite growth at ambient conditions have been previously studied, there is a lack of data on this at hydrothermal conditions. Our study, conducted at elevated temperatures and pressures in a triphasic gas–liquid–solid system, is meant to fill this gap. The experimental conditions used in this study are relevant for geological sequestration sites or geological systems associated with calcite carbonation reactions. Indeed, the mobility and/or uptake of Se and other trace elements contained in native rocks by mineral dissolution can be expected during CO_2 injection in geological formations (or any Ca-rich industrial waste), followed by carbonate precipitation (e.g. Kharaka et al., 2006). In general, hydrothermal conditions are representative of several geological environments in the Earth's upper crust where carbonate and selenium may interact: hydrothermal systems at mid-ocean ridges (Fouquet et al., 1996; Rouxel et al., 2004), black shales (Orberger et al., 2007), deep-seated plutonic rocks incorporating dense calcite vein networks (Malisa, 2001), coal beds (Yudovich and Ketris, 2006), and oil and gas reservoirs where CO_2 is used either as an enhanced oil recovery agent or for underground storage and sequestration (Kharaka et al., 2006).

The aim of the present study is the microscopic and molecular-scale characterization of calcite precipitated from an aqueous CO_2–H_2O–$Ca(OH)_2$ medium containing selenium at hydrothermal conditions. Similar experimental conditions were used in two previous studies, both with specific industrial applications: synthesis of a new calcite/Se^0 composite (Montes-Hernandez et al., 2008a) and removal of oxyanions from synthetic wastewater (Montes-Hernandez et al., 2009). The current study, however, is more fundamental in nature and provides new detailed data on calcite growth in the presence of inorganic and organic Se at hydrothermal conditions. This was achieved by using more sophisticated and higher resolution analytical tools: synchrotron X-ray absorption spectroscopy (XAS), high resolution transmission electron microscopy (HRTEM), and Field Emission Scanning Electron Microscopy (FESEM).

FESEM and HRTEM were used to study the morphology of the crystals, particle sizes, and the physical organization of the calcite nanoparticles. XAS was used to investigate the speciation and sorption/incorporation mechanism(s) of selenium in calcite. In addition, XAS was explicitly used to study the effects of certain physicochemical parameters, such as the initial concentration of the selenium compounds used (sodium selenite and seleno-L-cystine), temperature (30 and 90 °C), gas pressure (CO_2 or CO_2 + Ar mixture, at 20, 55 and 90 bar), and reaction time.

In the present study, novel insights have been gained concerning selenite incorporation into calcite structure, inhibition of calcite growth (leading to a nanostructured calcite), and irregular organization of nanosized crystallites. There are, however, several limitations to the present approach. Based on our experimental setup and on the ex-situ measurements (HRTEM and XAS), it remains difficult to determine whether the nanostructured calcite is the product of multiple nucleation events from a different precursor, such as amorphous calcium carbonate or vaterite. In order to shed more light on this, time resolved in situ measurements would be necessary, by coupling, for example, a reaction cell with XAS, RAMAN, or IR spectroscopic

techniques. Predictive numerical simulations (e.g. ab initio, Monte Carlo or geochemical codes) could also be used to gain a better understanding of these processes.

2. Materials and methods

2.1. Nucleation growth of calcite in presence of seleno-L-cystine

2.1.1. O_2-poor conditions/with purging

One liter of high-purity water with an electrical resistivity of 18.2 MΩ cm, 3 g of commercial portlandite $Ca(OH)_2$ (calcium hydroxide, Sigma-Aldrich, 96% chemical purity, with 3% $CaCO_3$ and 1% other impurities), and different masses (0, 50, 100 or 200 mg) of seleno-L-cystine, $CO_2HCH(NH_2)CH_2(Se)_2CH_2CH(NH_2)CO_2H$ (Sigma-Aldrich, chemical purity ≥98.0%) were placed in a stirred titanium reactor (stirred Parr® autoclave with internal volume of 2 L). The calcium hydroxide and the seleno-L-cystine particles were immediately dispersed in the solution by stirring (400 rpm). Argon gas (99.999% chemical purity, Linde Gas) was injected into the autoclave at room temperature and at a fixed pressure of 90 bars for 30 min. The aqueous suspension in the reactor was then heated to 90 °C. The pressure was maintained constant at 90 bars by successive manual purging until the temperature was stabilized (≈90 min). With respect to this protocol, we assumed that the injection of argon removed a substantial amount of the initial dissolved oxygen, resulting in O_2-poor conditions (we note that the reactor configuration did not permit the measurement of the pO_2 inside the reactor). The reactor was then subjected to flash purging until atmospheric pressure was reached. This was then followed by the injection of 14.5 g of CO_2 ($pCO_2 = 55$ bars, CO_2 with 99.995% chemical purity, Linde Gas). The total pressure in the system was immediately increased from 55 to 90 bars by argon injection. At these T and P conditions, the vapor phase primarily consists of an $Ar + CO_2$ mixture, with CO_2 in a supercritical state. The reaction time in these triphasic gas–liquid–solid experiments was typically 2 h, except for two selected experiments with durations of 5 and 15 days, respectively.

At the end of each experiment the reactor was rapidly depressurized (≈1 min) and the reactor fluid underwent rapid cooling from 90 to 35 °C over a time span of 15 min. The autoclave was then opened and disassembled, and the solid product was recovered after centrifugation (30 min at 12,000 rpm) and decantation of the supernatant solution. As a final step, the solid product was dried in centrifugation flasks for 72 h at 65 °C and then stocked in plastic flasks at ambient conditions.

2.1.2. O_2-rich conditions/no purging

For this experimental protocol, the aqueous suspension (water, calcium hydroxide, seleno-L-cystine, with compositions as described above) was heated to 90 °C at atmospheric pressure. When the temperature was stable, 14.5 g of CO_2 ($pCO_2 = 55$ bars) was injected into the reactor and the total pressure in the system was immediately adjusted to 90 bars by argon injection. The reaction durations and solid product recovery procedures were the same as described above for the O_2-poor protocol. An additional experiment was carried out using 200 mg of seleno-L-cystine at 30 °C and $pCO2 = 55$ bar (see Table 1). The only difference between O_2-poor and O_2-rich conditions is that no purging with argon was performed at O_2-rich conditions.

2.2. Nucleation growth of calcite in presence of selenite oxyanion (SeO_3^{2-})

One liter of high-purity water with an electrical resistivity of 18.2 MΩ cm, 20 g of commercial portlandite $Ca(OH)_2$ (96% chemical purity, with 3% $CaCO_3$ and 1% other impurities, Sigma-Aldrich), and three different masses (50, 100, 230 mg) of sodium selenite pentahydrate, $Na_2SeO_3.5(H_2O)$ (chemical purity>98%) were placed in a stirred titanium reactor (Parr® autoclave) with an internal volume of 2 L. The aqueous suspension was well mixed by stirring (400 rpm). The reactor containing the aqueous dispersion (solution charged with selenite oxyanion + Ca $(OH)_2$ particles in excess of its solubility) was then heated to 30 °C, and upon thermal stabilization, CO_2 (99.995% chemical purity, Linde Gas) was injected, until a pCO_2 of 20 bars was achieved (pCO_2 = total P of system). At these T and P conditions, the vapor phase consists mainly of CO_2 gas in an ideal state. After CO_2 injection, a pressure drop was visually followed on a manometer as a function of time until the pCO_2 reached an equilibrium value in this anisobaric gas–liquid–solid system. The rate of CO_2 transfer from the vapor to the aqueous dispersion was directly related to the concomitant drop in pCO2 and the formation of calcite in the fluid phase. For several experiments a pressure transducer (Keller series 33X) was interfaced with a PC computer, allowing for the continuous acquisition of the reactor pressure (see additional details in Montes-Hernandez et al., 2009). At the end of the experiment, the reaction cell was rapidly depressurized over approximately five minutes, followed by disassembly of the autoclave. Twenty milliliter of the suspension was immediately sampled and filtered in order to measure the pH and the selenium concentration. The solid product was recovered by centrifugation (30 min at 12,000 rpm) and decanting the supernatant solution. The last step consisted of drying the solid product for 72 h at 65 °C; the recovered material was stored at ambient conditions. In addition to the above conditions, an additional experiment with the same general protocol (using an initial concentration of sodium selenite of 230 mg/L) was carried out at 90 °C and $pCO_2 = 90$ bar (see Table 1).

Table 1
Proportions of Se species in calcite samples precipitated in the presence of selenocystine, determined by linear combination fits of EXAFS spectra.

Sample	Experimental conditions		Proportion of Se species (molar %)					
	Deviation from default conditions [a]	O_2 level	Se-cys	Red Se	Gray Se	Se (IV)	Sum	R factor $*10^{-2}$
Se1	None	O_2-poor	0	72	27	12	111	7.0
Se2	Washed	O_2-poor	0	49	53	9	111	4.4
Se3	9 mg Se/g calcite	O_2-poor	0	76	14	16	106	7.8
Se4	5 mg Se/g calcite	O_2-poor	0	47	23	28	97	9.4
Se19	55 bars, 30 °C	O_2-poor	30	43	–	9	82	8.5
Se20	10 days	O_2-poor	0	24	82	6	112	3.2
Se5	None	O_2-rich	0	16	76	16	107	5.7
Se7	9 mg Se/g calcite	O_2-rich	0	20	57	23	100	8.3
Se8	5 days	O_2-rich	0	12	75	13	101	6.7

[a] The default conditions are the following: the impurity is seleno-L-cystine, Se final content is 18 mg Se per g of calcite, pressure 90 bars, temperature 90 °C, and reaction time 2 h.

2.3. Scanning electron microscopy observations

The powder samples were dispersed by ultrasonic treatment in absolute ethanol for 5 to 10 min. One or two drops of the suspension were then deposited directly on a metal support for FESEM observations, with or without a metal coating. Morphological observations of various selected powders were performed using a Zeiss Ultra 55 field emission scanning electron microscope (FESEM) that has a maximum spatial resolution of approximately 1 nm at 15 kV.

2.4. Transmission electron microscopy measurements

Calcite crystals precipitated in the absence of selenium were examined using a JEOL 3010 transmission electron microscope (TEM) equipped with an energy dispersive X-ray analyzer (EDX). Calcite powder precipitated in

the presence of seleno-L-cystine was prepared for TEM by grinding in ethanol with an agate mortar and pestle, pipetting a drop of the suspension onto a TEM grid, and wicking away the excess solution. These samples were examined with a Jeol 2100F (field emission gun—FEG) instrument equipped with an energy EDX detector (ultrathin window, JEOL). TEM images were obtained at 200 kV in various imaging modes: bright field (BF), dark field (DF), scanning TEM - high angle annular dark field (STEM-HAADF). The latter technique, while not providing direct information on the chemistry, yields images with an elevated dependence on the atomic number (intensity $\propto Z^{3/2}$, where Z is the atomic number). Chemical maps were determined by EDX using the *K* lines for Ca, O, and C, and the *K* and *L* lines for Se.

2.5. X-ray absorption spectroscopy (XAS)

XAS measurements were carried out at the European Synchrotron Radiation Facility (ESRF, Grenoble, France), which was operating with a ring current of 100 mA. Se *K*-edge EXAFS spectra were collected on the BM30B (FAME) beamline using a Si(220) double crystal monochromator with dynamic sagittal focusing. The photon flux was of the order of 10^{12} photons per second, and the spot size was 300 μm horizontal × 100 μm vertical (Proux et al., 2006). The spectra were collected in transmission or fluorescence modes, depending on Se content. Se *K*α fluorescence was measured with a 30-element solid-state Ge detector (Canberra). Three to six scans of 40 min each were averaged. Data from each detector channel were inspected for glitches or drop-outs before inclusion in the final average.

The spectrum for gray (hexagonal) Se(0) was provided by A. Scheinost (Scheinost and Charlet, 2008). Amorphous (red) Se(0) reference was prepared by using a conventional reduction method of selenite (Na selenite pentahydrate purchased from Sigma). The reference and the Se-richest calcite samples were diluted in boron nitride. All samples were prepared as 5 mm diameter pellets, and were loaded in a helium cryostat with the temperature set to 10 K during data collection.

Data analysis was performed using the IFEFFIT package (Ravel and Newville, 2005), including ATHENA for the data extraction and linear combination fits (LCFs) and ARTEMIS for the shell fitting. For the normalization of the XANES data, the spectra were energy calibrated by setting the energy of the maximum of the white line for gray Se(0) at 12,659.2 eV. XANES spectra were normalized using polynomial functions of degrees 1 and 3 for the pre-and post-edge regions, respectively. For the extraction of EXAFS oscillations, E_0 was defined at the half height of the absorption edge step. For calcite samples synthesized in the presence of seleno-L-cystine (termed Secys), k^3-weighted EXAFS spectra were treated by LCFs in the 2–14.8 $Å^{-1}$ k range using Na selenite, gray Se(0), red amorphous Se(0), and Secys as fitting components. For calcite samples produced in the presence of sodium selenite, the spectra were treated by shell fitting. $k3$-weighted EXAFS spectra were Fourier transformed using a Kaiser–Bessel window ($\tau = 2.5$) over the k ranges 2.8–14.5 $Å^{-1}$ and 2.8–16.5 $Å^{-1}$, depending on the sample. Fits were performed on the Fourier filtered spectra over the R range 0.5–3.7 Å. Theoretical amplitude and phase shift functions for the atomic pairs Se–O, Se–Ca, and Se–Se were calculated with the *ab initio* code FEFF 6.0 (Rehr et al., 1991).

3. Results

3.1. Electron microscopy observations/measurements

3.1.1. Size and aggregation/agglomeration of calcite particles

In previous studies, microscopic observations revealed a preferential nucleation growth of sub-micrometric particles of calcite (<1 μm) with rhombohedral morphology at 90 °C and 90 bar (in absence of Se), whereas the preferential nucleation growth of nanometer-to-submicrometer size particles of calcite (<0.2 μm) with scalenohedral morphology was observed at 30 °C and 20–55 bar (in absence of Se) (Montes-Hernandez et al., 2008b). Conversely, the nucleation growth of calcite at 90 °C and 90 bar in the presence of seleno-L-cystine or sodium selenite clearly revealed a *c*-axial elongation of rhombohedral calcite crystals. In addition, an aggregation–agglomeration of calcite particles, leading to star-like morphologies was also observed in the presence of seleno-L-cystine (Montes-Hernandez et al., 2008a). In the present study, the shell-like morphologies (Fig. 1) and pseudo-amorphous aggregates (Fig. 2) were also observed by FESEM and TEM, respectively. Here, we provide new information on this type of aggregation–agglomeration process of calcite particles at a nanometer-to-micrometer scale, based on TEM measurements and observations that are detailed immediately below.

The presence of seleno-L-cystine proved to have an important influence on the type and distribution of crystal morphologies. Evidence for this is shown in Fig. 2, a STEM-HAADF image showing a representative population of calcite crystals, synthesized at 90 °C and 90 bar. Less than half of the precipitate population is composed of rhombohedra of uniform density, with diameters ranging from 0.5 to 1 μm. Fig. 2 also shows the presence of a few elongated, 8-sided scalenohedral crystals (2–4 μm in length); these crystals display the same uniform contrast as the rhombohedra, indicative of homogeneous density. The other

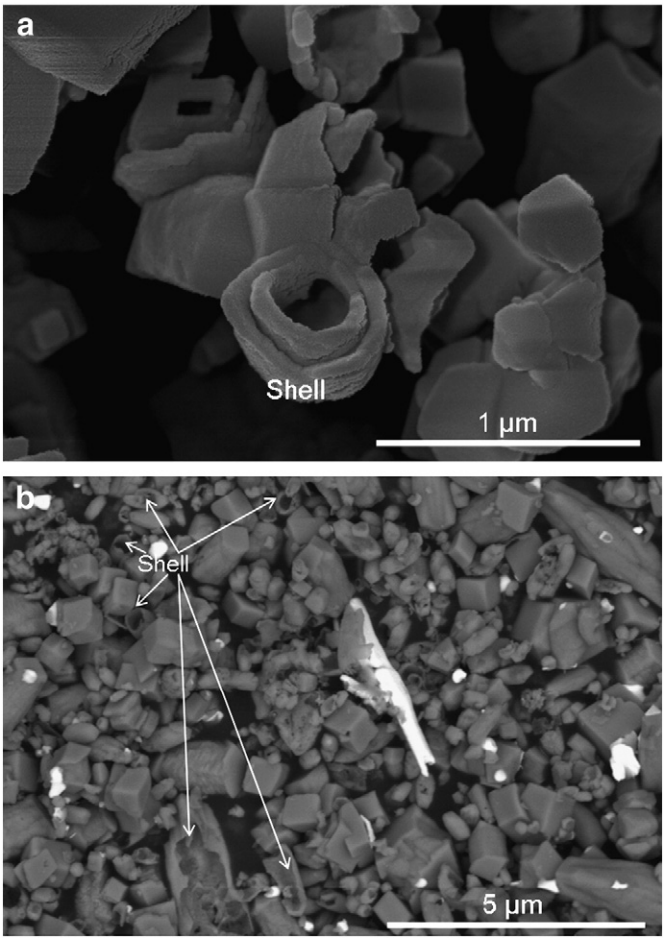

Fig. 1. Shell form for calcite produced in a triphasic gas–liquid–solid system in presence of seleno-L-cystine ($CO_2HCH(NH_2)CH_2(Se)_2CH_2CH(NH_2)CO_2H$) under high CO_2–Ar pressure (90 bar) and high temperature (90 °C). Note that the seleno-L-cystine was not chemically stable in basic pH solution; it was fragmented to elemental selenium (Se^0), selenite (SeO_3^{2-}), and in some cases to selenate (SeO_4^{2-}), depending on the amount of dissolved oxygen (for more details, see XAS measurements). a, FESEM image obtained via secondary electrons. b, FESEM micrograph obtained via backscattered electrons. Bright particles correspond to elemental selenium nanoparticles (Se^0).

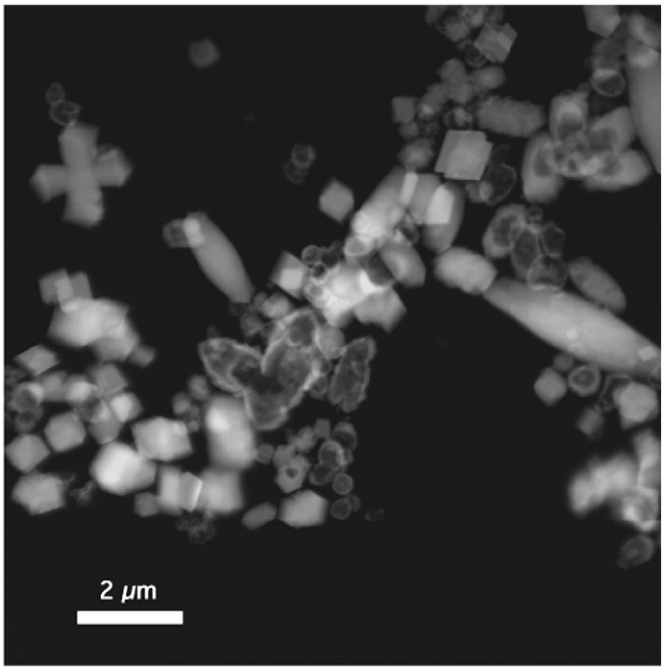

Fig. 2. STEM-HAADF image, showing a representative population of calcite crystals grown in the presence of seleno-L-cystine. Experimental conditions: P = 90 bar, T = 90 °C, O_2-poor conditions.

important population of precipitates (~50%) we designate as polycrystals, since they appear to be made of numerous, very small crystallites. The polycrystals are characterized by a spectrum of morphologies, and include irregular six- or eight-sided polygons with either elongated or equi-dimensional morphologies, sub-circular to oval forms, and completely irregular shapes. One of the defining characteristics of these particles is their apparent non-uniform density or thickness, as revealed by narrow rims with higher contrast.

Detailed measurements of the morphology and internal structure of the precipitated calcite particles were obtained at higher magnification, typical results are shown in Fig. 3. Fig. 3a, a STEM-HAADF image, and b, a BF TEM image, show two prismatic crystals with uniform contrast, and two polycrystals with heterogeneous contrast. The larger polycrystal clearly shows a rim and an elongated core region with an apparent higher density or thickness, and an interior region (between the core and rim) with an apparent lower density or thickness. It is interesting to note that even the interior region appears heterogeneous. The smaller, irregular polycrystal also has an apparent denser rim, but is lacking a denser core. The interior region appears to be more homogeneous, which is also evident in the STEM-HAADF image in Fig. 3a. Three selected area electron diffraction (SAED) diagrams were obtained at locations indicated in Fig. 3b, c; in all cases the spot size was on the order of 100 nm. The SAED diagram obtained from the circular area labeled 'd' on the rhombohedral crystal in Fig. 3b reveals the classic {104} habit. Two other SAED diagrams, obtained on the rim and in the interior of the small polycrystal (Fig. 3c), indicate the presence of single, monocrystalline domains. These domains, which correspond to individual crystallites approximately 100 nm in size, can be distinguished in the BF TEM image in Fig. 3c. There was no evidence of any amorphous material in the polycrystals. Within the analytical limits of SAED, the polycrystals appear to be mineralogically homogeneous and are constituted of calcite.

TEM images at higher magnification (Fig. 4a, b) reveal the polygonal nature and size distribution of the various crystallites making up each polycrystal. Fig. 4a shows two polycrystals with slightly different rim structures. The upper polycrystal has a rim composed of separate crystallites arranged in an en-echelon manner, with sizes on the order of several tens of nanometers. This type of rim structure was also

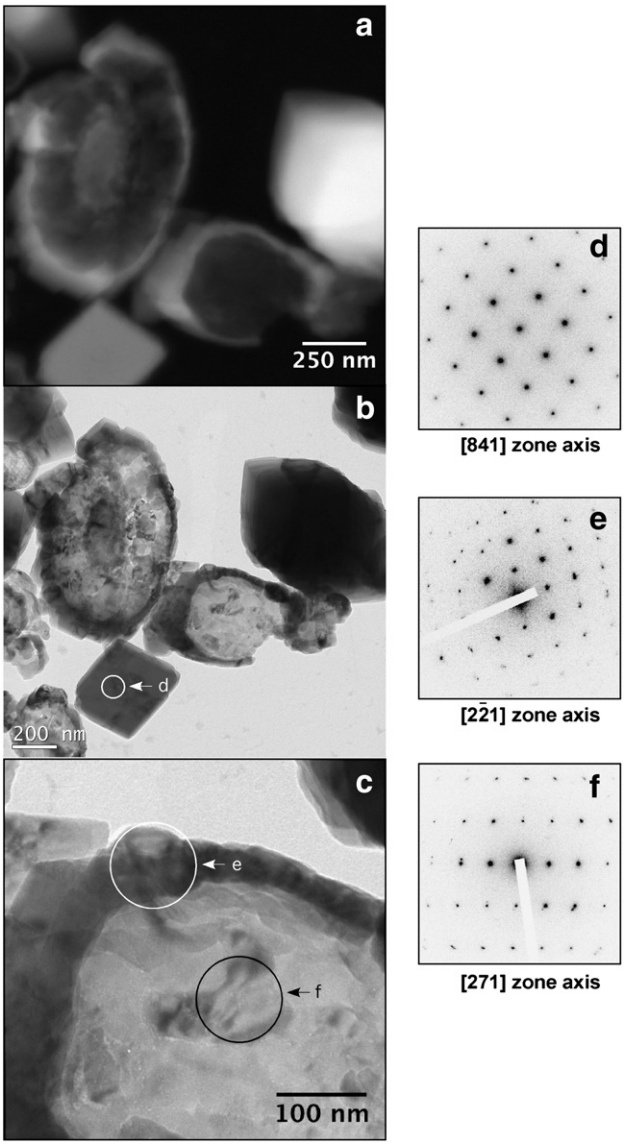

Fig. 3. TEM images of calcite monocrystals and polycrystals (a–c), including SAED diagrams (d–f, locations marked in b, c). a. STEM-HAADF image; note two prismatic crystals with uniform contrast, and two polycrystals with heterogeneous contrast. b. Bright field image c. Bright field image, representing enlargement of central polycrystal in panel b—note individual crystallites within the interior region approximately 100 nm in size d. SAED of calcite rhomodedron e. SAED of rim of polycrystal f. SAED of interior region. The SAED diagrams in e, f indicate the presence of single, mono-crystalline domains (100 nm spot size).

observed in other images (Fig. 3c). However, not all crystallites have this type of structure, as exemplified by the lower polycrystal in Fig. 4a, with a rim composed of concentrically oriented crystallites. The apparent density differences in the rim regions are most probably a thickness effect due to differential overlap of the crystallites. Note that in both polycrystals the interior regions appear to be composed of polygonal crystallites with variable contrast. As discussed further on, this is probably attributable (at least in part) to a lesser overall thickness of the interior regions of the polycrystals.

The indicated inset in Fig. 4a is shown at higher magnification in Fig. 4b, such that atomic resolution was achieved in this HRTEM image. A careful examination of the HRTEM image indicates the presence of multiple, individual nanometer size crystal domains (i.e. crystallites) that are characterized by differently oriented lattice fringes, areas of variable contrast, and Moiré fringes (due to overlap of differently oriented lattice fringes associated with individual crystallites). The crystallites,

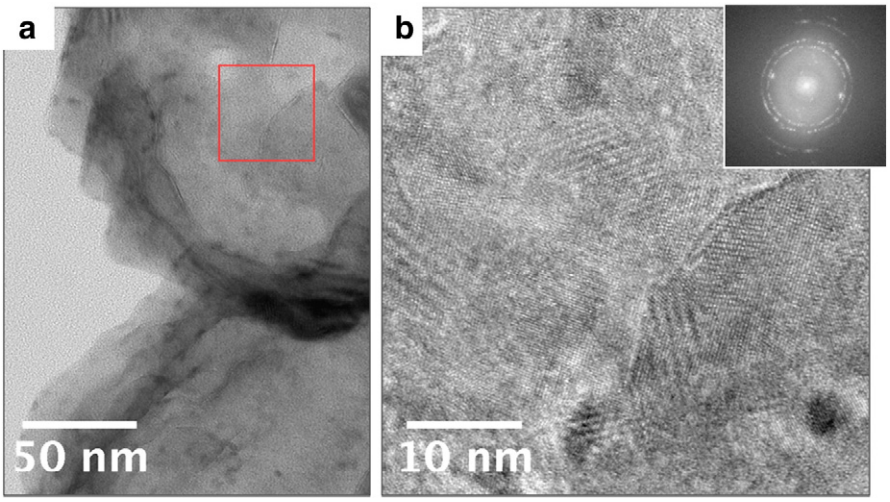

Fig. 4. Medium (a) and high resolution TEM images of a polycrystal. The HRTEM image in (b) shows presence of multiple individual crystallites, mostly in the 5–10 nm size range; note the presence of a larger (50 nm) crystallite occupying the entire bottom right portion of image, similar in size to those in Fig. 3c. The existence of nanoscale crystallites is also confirmed by the ring pattern of the Fast Fourier Transform (FFT) of the HRTEM image (shown in the inset of panel b).

characterized by polygonal geometries that are delimited by sharp boundaries, have a large spectrum of sizes. In Fig. 4b, the most important population of crystallites is in the 5–10 nm size range. The existence of nanometer size crystallites is also confirmed by the ring pattern of the Fast Fourier Transform (FFT) of the HRTEM image (shown in the inset to Fig. 4b). In the same figure, the bottom right part of the image is occupied by a single crystallite, approximately 50 nm in size, which is in the same size range as the large crystallites in Fig. 3b, c.

3.1.2. Elemental 2-D mapping with TEM-EDX

EDX chemical maps showing the distribution of Ca, C, O, and Se in a representative population of calcite precipitates are shown in Fig. 5a. For the purposes of comparison, Fig. 5a also portrays the corresponding BF TEM and STEM-HAADF images. In general, the three prominent rhombohedral crystals in Fig. 5a show relatively uniform concentrations of the four measured elements. Only the outer edges of the rims show fewer elemental counts. This is probably a thickness effect, since it is likely that the thickness of each crystal decreases towards the outer edges. In comparison, the polycrystals (easily identified by their dark rims in the BF image, or white rims in the STEM-HAADF image) have apparent non-uniform concentrations. All of the elements have apparent higher concentrations in the rims, and in certain polycrystals, in the core regions, as well (e.g. this is especially apparent in the Ca–K and O–K maps). The apparent concentrations of all elements measured in the rims and specific core regions of the polycrystals are less than the bulk concentrations measured in the rhombohedral crystals (Fig. 5a). Moreover, the interior regions of the polycrystals have apparent concentrations that are significantly less than in the rims, and even more so in comparison with the apparent concentrations in the rhombohedra.

With respect to the overall concentration distribution of Se in both the rhombohedra and the polycrystals, Fig. 5a reveals a positive correlation between Se and Ca, C, and O. However, Se also displays local areas where its concentration is significantly higher compared to the surrounding regions. In Fig. 5a the most prominent enrichment occurs in a local area (~70 nm diameter) associated with a crystallite. It is interesting to note that this Se-enriched zone does not correspond to a localized enrichment in Ca, Ca, or O. Other crystal/crystallite populations show more numerous areas of Se enrichment, as evidenced by a Se EDX map superposed on a STEM-HAADF image shown in Fig. 5b. In this image, Se enrichment is characterized by either a generalized enrichment encompassing an entire grain (white arrows, Fig. 5b), or by more pronounced enrichments restricted to much smaller localized areas (black arrows, Fig. 5b). The STEM-HAADF image in Fig. 5b reveals that the areas of generalized Se enrichment are associated with individual crystallites, and not prismatic monocrystals. The smaller, localized areas of Se enrichment are clearly associated with regions having diameters of ~80 nm (marked by black arrows on STEM-HAADF and EDX map, Fig. 5b). There is no apparent correlation between the areas of Se enrichment (generalized and localized) and the corresponding Ca, C, and O concentration distributions. This may indicate that areas of Se enrichment are not correlated with Se incorporation into the calcite structure, but rather represent the presence of elemental selenium or a Se-containing phase (but not carbonate) that is either adsorbed or precipitated onto the crystallite surfaces.

The measured concentration variations of Ca, O, C, and Se in the precipitated calcite crystals, in particular the variations measured in the polycrystals, can be partly attributed to a thickness effect, as shown in Fig. 6. Fig. 6a, an elastic (zero loss) TEM image, shows three overlapping polycrystals with characteristic rims and cores with higher apparent densities (except top most polycrystal with no dense core). Fig. 6b is the corresponding thickness image. As can be clearly seen, the thickness of each polycrystal is not uniform: the white regions indicate thicker regions (i.e. rim and core of central crystallite), compared to the thinner grey regions. Fig. 6c represents an EFTEM Ca map of the same polycrystals. The white and dark grey regions correspond to, respectively, higher and lower Ca counts. Note that the spatial distribution of the Ca counts correlates positively with the thickness map in Fig. 6b. From this result it is apparent that the polycrystals are characterized by thin interior regions and thicker rims, and in some cases, thicker cores as well. Non-uniform thicknesses are the probable reason for the differences in contrast that characterize the polycrystals imaged in Figs. 2–5, respectively. On the other hand, there is no evidence for a differential thickness effect associated with the localized regions of very elevated Se enrichment

Fig. 5. a. EDX chemical maps showing the distribution of Ca, C, O and Se in a representative population of crystals and polycrystals (element given in upper left corners, higher concentrations correspond to higher counts and brighter colors). Corresponding BF TEM (lower left) and STEM-HAADF (lower right) images. Panel b. STEM-HAADF and corresponding Se EDX map superposed on a HAADF image showing Se counts. Black arrows designate areas of localized enrichment, white arrows diffuse enrichment. Note that Se is preferentially localized in calcite polycrystals, and not in the monocrystals.

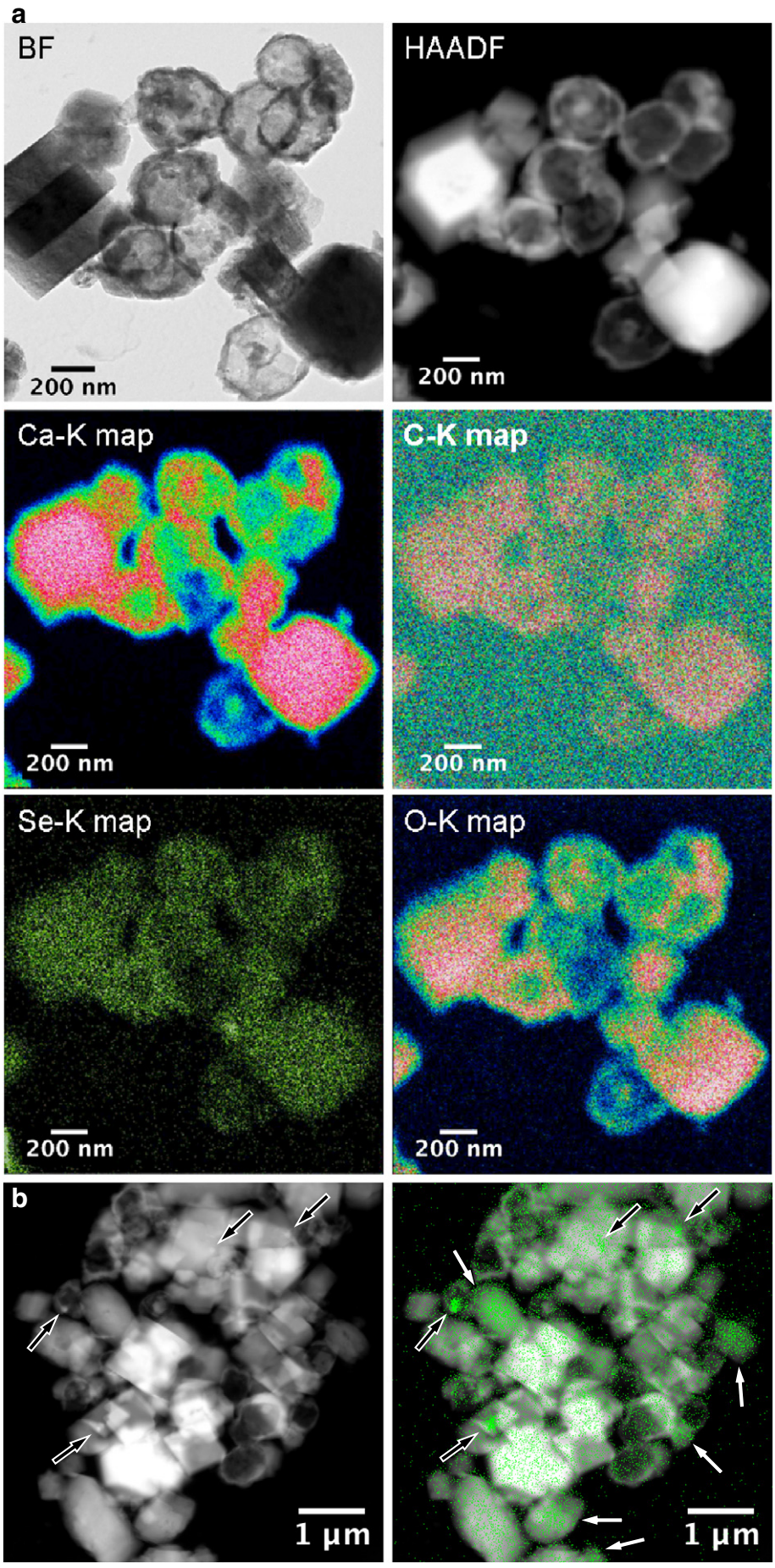
a
BF
200 nm
HAADF
200 nm
Ca-K map
200 nm
C-K map
200 nm
Se-K map
200 nm
O-K map
200 nm
b
1 μm
1 μm

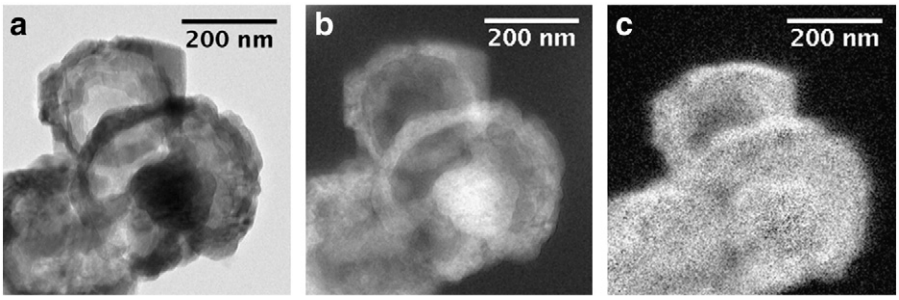

Fig. 6. (a) Elastic (zero loss) TEM image showing three overlapping polycrystals with characteristic rim and cores with higher apparent densities (except top most crystallite without a dense core). (b) Corresponding thickness image. (c) Calcium EFTEM map of the same crystallites (white areas denote higher Ca counts).

imaged in Fig. 5b. These deductions are clearly in agreement with the FESEM observations (Fig. 1b).

3.2. XAS measurements

3.2.1. Se speciation in calcite grown in presence of the seleno-L-cystine

Fig. 7 shows the Se *K*-edge EXAFS spectra for the calcite samples that formed in the presence of seleno-L-cystine. The spectra for samples Se5, Se7, Se8, and Se20 clearly resemble the gray Se^0 spectrum, whereas spectra for Se1, Se3, and Se4 present more similarities with red amorphous Se^0. The spectrum for Se19 has lower amplitude compared to Se1, Se3, and Se4, and is closer to the seleno-L-cystine reference. The spectrum from the reference compound is dominated by a Se–Se interaction with a single Se neighbor, whereas in gray and red Se^0, the first shell contains two Se atoms. The experimental conditions of synthesis for samples Se1 to Se8, Se19, and Se20 are summarized in Table 1.

Results of the linear combination fits (LCFs) are given in Table 1 and in Fig. 8, after normalization of the values to 100%. All spectra were correctly simulated by a combination of gray Se^0, red amorphous Se^0, and selenite, except spectrum Se19, for which a better fit was obtained with a combination of selenocystine, red amorphous Se^0, and selenite.

Sample Se19 differs from the others because it corresponds to conditions at lower pressure and temperature conditions (30 °C and 55 bars, Table 1). These moderate conditions seem to have partially preserved the selenocystine and resulted in its sorption onto calcite (since it was present on the calcite samples after centrifugation), whereas this compound was completely transformed at higher *T* and *P* conditions (see Table 1 and Fig. 8). Sample Se2 contains a lower percentage of red amorphous Se^0 compared to sample Se1. A possible interpretation is that some nanoparticles of red Se^0 remained in suspension during the washing procedure (contrary to larger gray Se particles), thus they were removed from the solid phase during this step. A comparison of Se1 *vs.* Se5, and Se3 *vs.* Se7, shows that the O_2-poor conditions favored the formation of red Se^0, whereas O_2-rich conditions favored the formation of gray Se^0.

The formation of selenite appears to have been favored in samples Se4 and Se7, which contain less Se than samples Se1 and Se5, respectively. This higher content in selenite is also attested to by a peak on the XANES spectrum at about 12,665 eV, which is the position of the principal selenite peak (Fig. SI-1 in supplementary information), and by a peak in the Fourier transformed spectra corresponding to an oxygen shell (not shown). Sample Se3 is intermediate between Se1 and Se4 in terms of Se content and percentage of selenite. Therefore, there seems to be a negative correlation between Se content and the formation of Se(IV), observed both in O_2-poor and O_2-rich conditions.

Finally, a comparison of Se1 *vs.* Se20 shows an increase in the proportion of gray Se^0 vs. red Se^0 with time in O_2-poor conditions. This time effect was not observed after 5 days at O_2-rich conditions, as shown by the comparison of Se5 and Se8 samples (note that sample Se5 was already primarily composed of gray Se^0).

3.2.2. Se speciation in calcite grown in the presence of selenite oxyanion

The EXAFS spectra for the calcite precipitated in the presence of sodium selenite pentahydrate are shown in Fig. 9. They differ from the previous calcites grown in the presence of seleno-L cystine. LCFs using the four reference spectra shown in Fig. 7 did not provide satisfactory results, therefore suggesting the presence of another Se

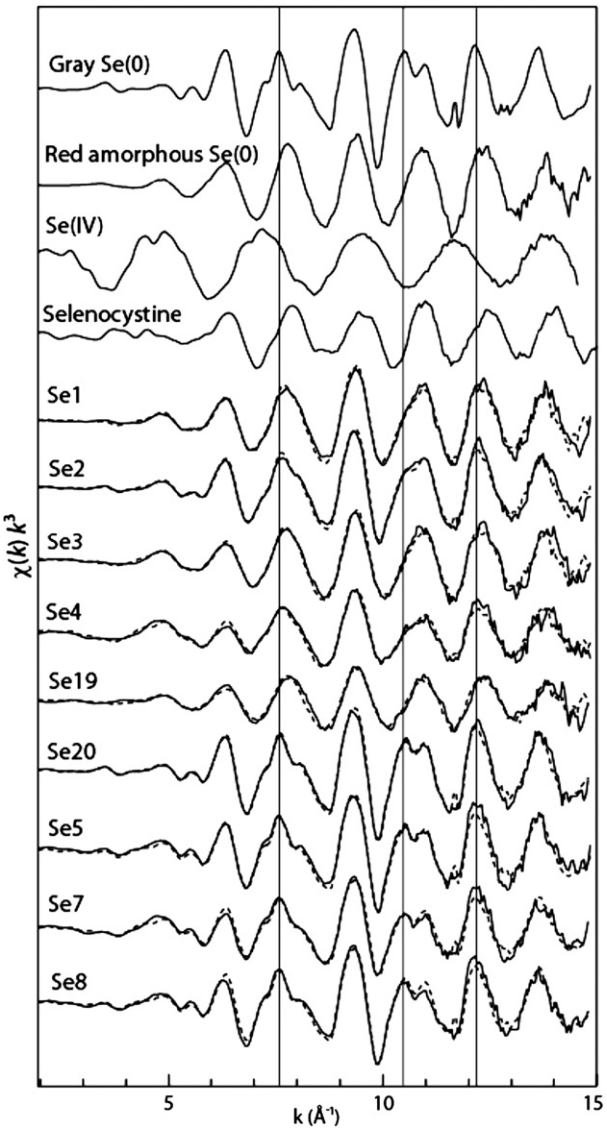

Fig. 7. k^3-weighted EXAFS spectra for reference compounds and calcite samples produced in the presence of selenocystine. Solid lines: experimental; dashed lines: linear combination fits.

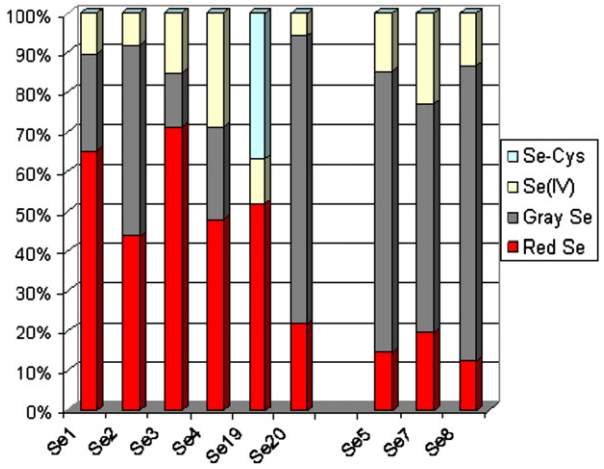

Fig. 8. Proportion of Se species determined by LCFs of EXAFS spectra after normalisation of the values given in Table 1 to 100%.

species. The spectra present high frequency contributions that increase in the order: Se18<Se9<Se10<Se11<Se12<Se13 (insets in Fig. 9). The Fourier transformed spectra show a first peak characteristic of oxygen neighbors, which was simulated by 2.4 to 2.7 oxygen atoms at 1.70 Å (Table 2). This suggests that Se is present as selenite, which is confirmed by the position of the absorption edge (Fig. SI-1c in supplementary information). The fact that the number of oxygen atoms is slightly below 3 may indicate some structural disorder due to slightly different geometries of the Se sorption sites. The FTs show a second peak of varying amplitude depending on the sample. For sample Se9, the peak is clearly split and was fitted by 1.5 Ca atoms at 3.31 Å and 3.0 Ca atoms at 3.53 Å (Table 2). Two Ca sub-shells were also found for Se18. For the other samples (Se10 to Se13), a third Ca sub-shell was added to the fit. This additional Ca sub-shell contained 0.7 to 1.0 Ca atom located at a shorter distance (3.02–3.04 Å) than the two main Ca sub-shells (3.26–3.31 Å and 3.53–3.54 Å). Fig. 10 compares the fits for SE13 with two and three Ca sub-shells. Although the former is relatively satisfactory, the latter allows a very good reproduction of the second peak. With this additional shell, the number of independent parameters is still much higher than the number of variables (24 and 11, respectively). The total number of Ca atomic neighbors varies from 3.8 to 6.0 in samples Se10 to Se13. The presence of six Ca atomic neighbors is consistent with a substitution of carbonate anion by selenite oxyanion in the calcite structure. The CO_3^{2-} anion is planar, and in calcite the C atom is surrounded by six Ca neighbors at the same distance (3.213 Å). On the other hand, the SeO_3^{2-} oxyanion is pyramidal, such that if we suppose that the three oxygen atoms remain in the same position, Se would then be shifted out of the center of the Ca octahedron. The occurrence of two or three Ca sub-shells depends on the direction of the shift of Se relative to the C position. A shift of 0.3 Å along the *c* axis would lead to two Ca sub-shells of three atoms each at 3.09 and 3.36 Å, whereas a shift of 0.1, 0.1, and 0.3 Å along the ortho-normal axis would lead to three Ca sub-shells of two atoms each at 3.03, 3.22, and 3.42 Å (Fig. 11). These distances are not too different from those obtained by EXAFS, although the atoms are not distributed equally among the three sub-shells. We therefore deduce that in samples Se10 to Se13, selenite is incorporated in calcite, and Se atoms are displaced relative to the position of C atoms not only along the *c* axis but along the *a* and *b* axes, as well. The number of Ca neighbors decreases with increasing Se content, i.e., from samples Se12, 13 to samples Se9, 10, 11, and 18. This decrease might reflect the presence of additional sorbed species with increasing Se content. The structural parameters are almost identical in Se10 and Se11 (Se10 after washing), suggesting that sorbed species for this particular sample are not readily exchangeable at this concentration.

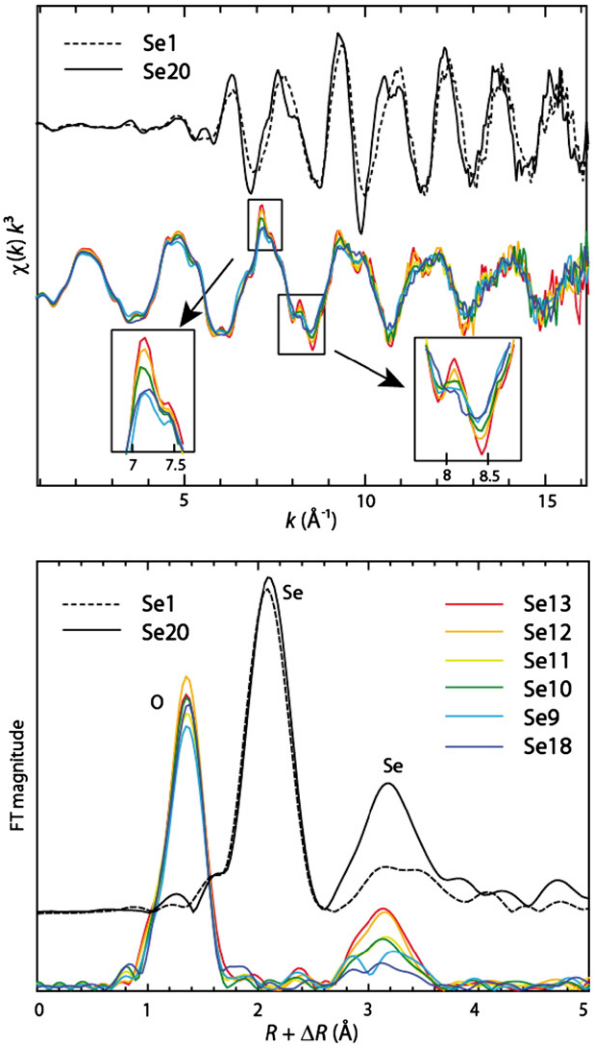

Fig. 9. The EXAFS spectra for the calcite samples produced in presence selenite as impurity. The Fourier transformed spectra showing a first peak characteristic of oxygen neighbors, which was simulated by 2.4 to 2.7 oxygen atoms at 1.70 Å. It indicates that Se is present as selenite.

4. Discussion

4.1. Nucleation growth of nanostructured calcite

The results from the present study clearly reveal that the structural incorporation of selenite oxyanion in calcite results in a *c*-axial elongation of rhombohedral crystals. Moreover, it also produces a disordered aggregation of rhombohedral nano-crystals, leading to irregular calcite polycrystals. There was no evidence of any amorphous material in the polycrystals. Note that amorphous calcium carbonate and metastable crystalline phases of $CaCO_3$ (such as vaterite and aragonite) are frequently considered to be calcite precursors in aqueous media. The formation of these solid metastable phases could be enhanced by the presence of certain aqueous species or additives. For example, a recent study claimed that a high initial concentration of Se(IV) (1.2 mmol/L) suppressed the formation of calcite and led to vaterite precipitation at atmospheric conditions using a classic homogeneous system (i.e., solution–solution interactions) (Aurelio et al., 2010). Conversely, in the present study at hydrothermal conditions using a triphasic gas–liquid–solid system, only calcite was observed to form in the presence of similar initial concentrations of Se(IV) (1 mmol/L). Another remarkable difference between these studies was the

Table 2
Structural parameters for reference compounds and for calcite samples precipitated in the presence of Na selenite.

Sample	Deviation from default conditions	Atom	R (Å)	N	$N_{Ca\ tot}$	σ^2 (Å^2)	R factor$*10^{-2}$
Red amorphous Se^0		Se	2.35 ± 0.005	2.6 ± 0.2		0.004	1.2
		Se	3.70 ± 0.02	0.9 ± 0.3		0.004	
Gray Se^0		Se	2.38 ± 0.006	2.0 ± 0.2		0.003	3.0
		Se	3.39 ± 0.01	4.0 ± 0.2		0.007	
		Se	3.73 ± 0.02	2.0 ± 0.2		0.007	
Na selenite		O	1.71 ± 0.006	3.0 ± 0.2		0.002	1.4
Se9	90 bars, 90 °C	O	1.70 ± 0.005	2.5 ± 0.1		0.002	2.7
		Ca	3.31 ± 0.02	1.5 ± 0.5	4.5 ± 1.3	0.005	
		Ca	3.53 ± 0.02	3.0 ± 0.8		0.008	
Se10	4.6 mg Se/g calcite	O	1.70 ± 0.004	2.7 ± 0.1		0.002	2.6
		Ca	3.03 ± 0.04	0.6 ± 0.5	3.8 ± 2.2	0.005	
		Ca	3.26 ± 0.02	1.5 ± 0.9		0.005	
		Ca	3.54 ± 0.02	1.7 ± 0.8		0.005	
Se11	4.6 mg Se/g calcite, washed	O	1.70 ± 0.004	2.5 ± 0.2		0.002	2.3
		Ca	3.01 ± 0.03	0.7 ± 0.5	4.2 ± 2.1	0.005	
		Ca	3.26 ± 0.02	1.6 ± 0.8		0.005	
		Ca	3.53 ± 0.02	1.8 ± 0.8		0.005	
Se12	2.5 mg Se/g calcite	O	1.70 ± 0.002	2.8 ± 0.2		0.002	1.8
		Ca	3.04 ± 0.03	0.8 ± 0.7	5.7 ± 3.9	0.005	
		Ca	3.27 ± 0.01	2.4 ± 1.7		0.005	
		Ca	3.53 ± 0.01	2.5 ± 1.5		0.005	
Se13	1.3 mg Se/g calcite	O	1.70 ± 0.002	2.7 ± 0.2		0.002	2.1
		Ca	3.03 ± 0.03	0.8 ± 0.6	6.0 ± 1.5	0.005	
		Ca	3.27 ± 0.01	2.4 ± 0.4		0.005	
		Ca	3.54 ± 0.01	2.8 ± 0.5		0.005	
Se18	Ca source: paper mill waste	O	1.70 ± 0.004	2.6 ± 0.2		0.002	1.9
		Ca	3.30 ± 0.03	0.7 ± 0.4	2.3 ± 1.1	0.005	
		Ca	3.54 ± 0.03	1.6 ± 0.7		0.008	

The default conditions are the following: the impurity is selenite, the Ca source is portlandite, Se final content is 20 mg Se per g of calcite, pressure 20 bars, temperature 30 °C, and reaction time 2 h. R: Interatomic distance, N: Number of atoms, $N_{Ca\ tot}$: Number of Ca atoms, σ^2: Debye Waller factor, R factor = normalized sum squares. For Se9 and Se18, the Debye–Waller factors for the three Ca shells were fixed. For Se10 to Se13, the Debye–Waller factors for the three Ca shells were set equal. The error bars were calculated using ARTEMIS software from the diagonal of the covariance matrix (Ravel and Newville, 2005).

particle size: micrometric carbonate particles were generally observed under atmospheric conditions (e.g., Aurelio et al., 2010), wheras sub-micrometric single calcite particles and polycrystals composed of nanometer-sized calcite crystallites (nanostructured calcite) were observed in the present study at hydrothermal conditions.

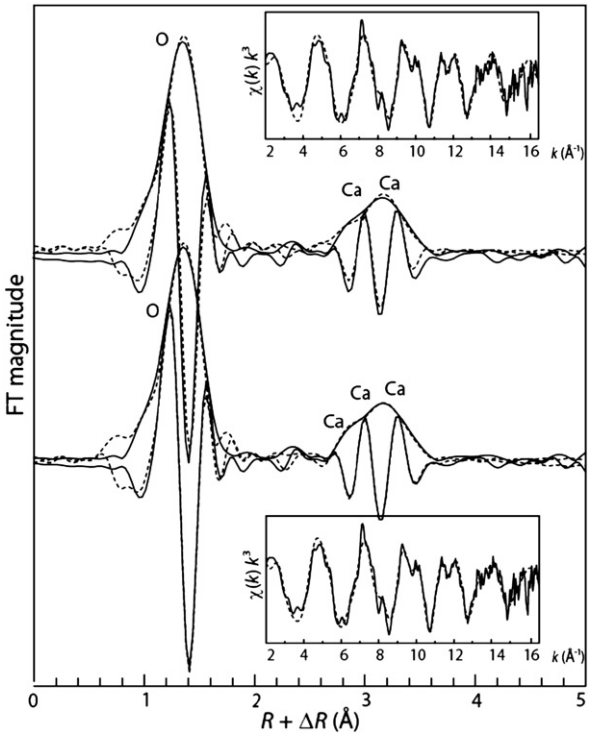

Fig. 10. Shell fitting for sample Se13 with two (top) and three (bottom) Ca sub-shells. Fourier transformed (modulus and imaginary part) and k^3-weighted EXAFS spectra (inset) are shown. Solid lines: experimental; dashed lines: fits.

Our results based on the detailed TEM measurements on calcite revealed a very complex effect of seleno-L-cystine on the particle size and the aggregation–agglomeration process. As already detailed, we observed several types of morphologies: rhombohedra, elongated rhombohedra (c-axis elongation), scalenohedra, star-like crystal aggregates, and irregular calcite polycrystals. As above mentioned, the seleno-L-cystine (amine-acid) molecule was not chemically stable during calcite growth; it was chemically fragmented since the selenium was oxidized from Se(–II) (in seleno-L-cystine) to Se(0) and Se(IV) under O_2-poor conditions, and to Se(0), Se(IV) and Se (VI) under O_2-rich conditions (see also Montes-Hernandez et al., 2008a). The fate of the remaining organic residue during calcite growth is unclear. In our study, EXAFS measurements using linear combination fits have only revealed that selenocystine was not present in the solid product except at a lower temperature (30 °C) (see Fig. 8). Moreover, in a previous study (Montes-Hernandez et al., 2008a, 2008b), HPLC coupled to ICP-MS was used to measure the residual seleno-L-cystine in solution during the carbonation process—this revealed rapid consumption, such that it was no longer measurable after 1 h of reaction (see Table 1 in Montes-Hernandez et al., 2008a). However, this organic matter may be responsible for the star-like and shell-like crystal aggregates, as these morphologies were not observed when calcite was grown in presence of selenite oxyanion (Se(IV)). Thus, the formation of nanostructured calcite material can be explained by the classic theory of crystal growth inhibition: the surfaces of calcite nuclei were poisoned by the incorporation of selenite (SeO_3^{-2}) and by the presumed adsorption of other unidentified organic impurities produced in situ during seleno-L-cystine chemical fragmentation. It is well-known that certain aqueous species and additives in solution can modify crystal growth habits and induce crystallographic twinning by sorption of these species to

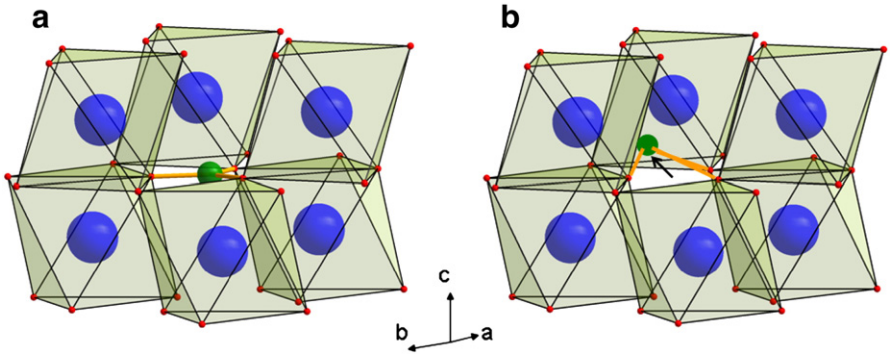

Fig. 11. a) Detail of calcite structure showing a CO_3 group coordinated by six Ca atoms. b) Possible environment for the SeO_3 substituting in a CO_3 position. Se is shifted along *a*, *b* and *c* relative to the position of C in calcite. Ca: blue, O: red, C and Se: green.

the growing crystal surfaces, thereby inhibiting their growth kinetics. Our high resolution electron microscopy results (HRTEM) have clearly revealed that inhibition of calcite crystal growth favors the nucleation process (i.e., an increase in the concentration of particles), this leading to the irregular aggregation of nanoparticles (<100 nm) and/or the formation of nanostructured calcite material.

4.2. Evidence for selenite (SeO_3^{2-}) incorporation into the calcite structure

Based on the XAS data analysis of calcite grown in the presence of selenite, Se is incorporated into the calcite structure via the substitution of selenite anion (SeO_3^{2-}) for carbonate anion. Previous studies have also shown the substitution of various (tetrahedral) oxyanions into the calcite structure. Reeder et al. (1994) have shown that selenate (SeO_4^{2-}) oxyanion substituted for carbonate in calcite coprecipitated at room temperature. They found that Se(VI) was surrounded by 2 Ca atoms at 3.17 Å and approximately 4 Ca atoms at 3.49 Å, and proposed two possible configurations for the selenate tetrahedron, with corner sharing of each SeO_4 tetrahedron with neighboring Ca octahedra. Other tetrahedral oxyanions, including CrO_4^{2-} and AsO_4^{3-}, were found to substitute for CO_3^{2-} in calcite (Alexandratos et al., 2007; Tang et al., 2007). In all of these cases, the metal(loïd) was off-centered compared to the C position. Cheng et al. (1997) studied the sorption of selenite on the calcite (104) surface. They observed the replacement of CO_3^{2-} by SeO_3^{2-} anion, with no diffusion of selenite towards the crystal bulk or epitaxial growth. Aurelio et al. (2010) studied calcite coprecipitated with selenite at atmospheric conditions. The Ca peak was modeled by two Ca sub-shells at 3.25 and 3.53 Å. They found a total of three neighboring Ca atoms, whereas in the present study, up to six Ca atomic neighbors were found. It is important to note that the better signal-to-noise ratio of our spectra allowed us to include a third Ca sub-shell for some samples, which better reproduced the Ca peak. A total of six Ca neighbors (observed in samples Se12 and Se13) are consistent with a single site for Se, i.e., selenite being substituted for carbonate in the calcite structure. The presence of three Ca sub-shells suggests that Se is not only shifted along the *c* axis, but also that the pyramid is slightly tilted relative to this axis. The weaker contribution of the Ca shell observed in the most concentrated samples suggests the presence of additional species, possibly selenite sorbed at the calcite surface.

5. Conclusions

Within the first few kilometers of the Earth's upper crust, reactive fluids containing calcium and selenium will interact during carbonation processes, in particular in environments characterized by high thermal gradients, such as in hydrothermal systems at mid-ocean ridges or in deep-seated plutonic rocks. In addition, lithologies with elevated organic contents (black shales, coal beds, and hydrocarbon reservoirs) also favor Ca and Se interactions during carbonation. Thus, one of the fundamental processes associated with the overall Se cycle is its incorporation into carbonates, in particular calcite. This study provides new data on the role of Se in carbonation processes in hydrothermal environments. In particular, we show how calcite precipitated from CO_2–H_2O–$Ca(OH)_2$ solutions is modified by the presence of organic and inorganic selenium. Our study elucidates the specific effects of Se incorporation in the calcite crystal structure in terms of crystal size, structural order (crystallinity), morphology of crystal faces, crystal organization, and selenium speciation.

The use of synchrotron XAS and electron microscopy (FESEM and TEM) allowed us to achieve novel and fundamental nanoscale measurements of precipitated calcite incorporating Se. Shell fitting of EXAFS spectra, with respect to calcite grown in the presence of selenite oxyanion, showed clear evidence for the incorporation of selenite oxyanion (SeO_3^{2-}) into calcite crystals, i.e., carbonate anions (CO_3^{-2}) were replaced by selenite anions during calcite nucleation growth. At a low Se content (1.3 mg/g), a single site was observed with Se surrounded by six Ca atoms, whereas additional sites, probably surface sorption sites, were found with increasing Se content. Conversely, EXAFS spectra for calcite grown in the presence of seleno-L-cystine (Secys) were successfully analyzed by linear combination fits (LCFs). We also demonstrated that Secys was chemically fragmented during calcite nucleation growth, because the solid phase contained primarily elemental Se (hexagonal or amorphous form), with some oxidized Se (IV). Complementary measurements performed by electron microscopy (FESEM and TEM) on calcite revealed the presence of surface particles rich in selenium, in the form of elemental Se. In addition, TEM showed a very complex effect of seleno-L-cystine on the particle size and the aggregation–agglomeration process. This resulted in various calcite morphologies: rhombohedra, elongated rhombohedra (*c*-axis elongation), scalenohedra, star-like and shell-like crystal aggregates, and irregular calcite polycrystals. The fate of the remaining organic residue during the carbonation process is unclear. However, we speculate that this organic matter may be responsible for the star-like and shell-like crystal aggregates, because these morphologies were not observed with respect to the calcite samples grown in presence of selenite oxyanion (Se(IV)). Finally, the electron microscopy results (HRTEM) clearly revealed that inhibition of calcite crystal growth enhances the nucleation process (i.e., an increase in particle number concentration), leading to an irregular aggregation of nanoparticles (diameters <100 nm) or formation of nanostructured calcite material.

Acknowledgements

The authors are grateful to the French National Research Agency, ANR (GeoCarbone-CARBONATATION), Joseph Fourier University (Grenoble I),

and the CNRS for providing financial support. We acknowledge the ESRF for beam time and the FAME beamline team for their assistance during the XAS measurements. Laura Leone (LGIT, Grenoble) is acknowledged for the synthesis of red Se(0) reference material used for the XAS measurements and Andreas Scheinost (ESRF) for providing the diffraction spectrum of hexagonal Se(0).

Appendix A. Supplementary data

Supplementary data to this article can be found online at doi:10.1016/j.chemgeo.2011.09.007.

References

Alexandratos, V.G., Elzinga, E.J., Reeder, R.J., 2007. Arsenate uptake by calcite: macroscopic and spectroscopic characterization of adsorption and incorporation mechanisms. Geochimica et Cosmochimica Acta 71, 4172–4187.

Aurelio, G., Fernandez-Martinez, A., Cuello, G.J., Roman-Ross, G., Alliot, I., Charlet, L., 2010. Structural study of selenium (IV) substitutions in calcite. Chemical Geology 270, 249–256.

Cheng, L., Lyman, P.F., Sturchio, N.C., Bedzyk, M.J., 1997. X-ray standing wave investigation of the surface structure of selenite anions adsorbed on calcite. Surface Science 382, L690–L695.

Cheng, L., Fenter, P., Sturchio, N.C., Zhong, Z., Bedzyk, M.J., 1999. X-ray standing wave study of arsenite incorporation at the calcite surface. Geochimica et Cosmochimica Acta 63, 3153–3157.

Chrissanthopoulos, A., Tzanetos, N.P., Andreopoulou, A.K., Kallitsis, J., Dalas, E., 2005. Calcite crystallization on oxadiazole-terpyridine copolymer. Journal of Crystal Growth 280, 594–601.

Dalas, E., Chalias, A., Gatos, D., Barlos, K., 2006. The inhibition of calcium carbonate crystal growth by the cysteine-rich Mdm2 peptide. Journal of Colloid and Interface Science 300, 536–542.

Dousi, E., Kallitsis, J., Chrissanthopoulos, A., Mangood, A.H., Dalas, E., 2003. Calcite overgrowth on carboxylated polymers. Journal of Crystal Growth 253, 496–503.

Dove, P.M., Hochella, J.R.M.F., 1993. Calcite precipitation mechanisms and inhibition by orthophosphate: in situ observation by scanning force microscopy. Geochimica et Cosmochimica Acta 57, 705–714.

Fernandez-Martinez, A., Charlet, L., 2009. Selenium bioavailability and cycling in the environment: a structural chemist's point of view. Reviews in Environmental Science and Biotechnology 8, 81–110.

Fouquet, Y., Knott, R., Cambon, P., Fallick, A., Rickard, D., Desbruyeres, D., 1996. Formation of large sulfide mineral deposits along fast spreading ridges. Example from off-axial deposits at 12°43?N on the East Pacific Rise. Earth and Planetary Science Letters 144, 147–162.

Freij, S.J., Putnis, A., Astilleros, J.M., 2004. Nanoscale observations of the effect of cobalt on calcite growth and dissolution. Journal of Crystal Growth 267, 288–300.

Fujita, Y., Redden, G.D., Ingram, J., Cortez, M.M., Ferris, G., Smith, R.W., 2004. Strontium incorporation into calcite generated by bacterial ureolysis. Geochimica et Cosmochimica Acta 68, 3261–3270.

Gower, L.A., Tirell, D.A., 1998. Calcium carbonate films and helices growth in solutions of poly(aspartate). Journal of Crystal Growth 191, 153–160.

Heberling, F., Denecke, M.A., Bosbach, D., 2008. Neptunium(V) coprecipitation with calcite. Environmental Science and Technology 42, 471–476.

Jonasson, R.G., Rispler, K., Wiwchar, B., Gunter, W.D., 1996. Effect of phosphanate inhibitors on calcite nucleation kinetics as a function of temperature using light scattering in an autoclave. Chemical Geology 132, 215–225.

Kharaka, Y.K., Cole, D.R., Hovorka, S.D., Gunter, W.D., Knauss, K.G., Freifeld, B.M., 2006. Gas–water–rock interactions in the? Frio Formation following CO_2 injection: implications for the storage of greenhouse gases in sedimentary basins. Geology 34, 577–580.

Lackner, K.S., Wendt, C.H., Butt, D.P., Sharp, D.H., Joyce, E.L., 1995. Carbon dioxide disposal in carbonate minerals. Energy 20, 1153–1170.

Lee, Y.J., Reeder, R.J., 2006. The role of citrate and phthalate during Co(II) coprecipitation with calcite. Geochimica et Cosmochimica Acta 70, 2253–2263.

Levander, O.A., Burk, R.F., 2006. Update of human dietary standards for selenium. Its molecular biology and role in Human Health. Springer US, New York, pp. 399–410.

Malisa, E.P., 2001. The behaviour of selenium in geological processes. Environmental Geochemistry and Health 23, 137–158.

Martens, D.A., Suarez, D.L., 1997. Mineralization of selenium-containing amino acids in two California soils. Soil Science Society of America Journal 61, 1685–1694.

Menadakis, M., Maroulis, G., Koutsoukos, P.G., 2007. A quantum chemical study of doped $CaCO_3$ (calcite). Computational Materials Science 38, 522–525.

Montes-Hernandez, G., Renard, F., Geffroy, N., Charlet, L., Pironon, J., 2007. Calcite precipitation from CO_2–H_2O–$Ca(OH)_2$ slurry under high pressure of CO_2. Journal of Crystal Growth 308, 228–236.

Montes-Hernandez, G., Fernandez-Martinez, A., Charlet, L., Renard, F., Scheinost, A.C., Bueno, M., 2008a. Synthesis of a Se^0/calcite composite using hydrothermal carbonation of Ca$(OH)_2$ coupled to a complex selenocystine fragmentation. Crystal Growth and Design 8, 2497–2504.

Montes-Hernandez, G., Fernandez-Martinez, A., Charlet, L., Tisserand, D., Renard, F., 2008b. Textural properties of synthetic calcite produced by hydrothermal carbonation of calcium hydroxide. Journal of Crystal Growth 310, 2946–2953.

Montes-Hernandez, G., Concha-Lozano, N., Renard, F., Quirico, E., 2009. Removal of oxyanions from synthetic wastewater via carbonation process of calcium hydroxide: applied and fundamental aspects. Journal of Hazardous Materials 166, 788–795.

Montes-Hernandez, G., Daval, D., Chiriac, R., Renard, F., 2010. Growth of nanosized calcite through gas–solid carbonation of nanosized portlandite particles under anisobaric conditions. Crystal Growth and Design 10, 4823–4830.

Nehrke, G., Reichart, G.J., Van Cappellen, P., Meile, C., Bijma, J., 2007. Dependence of calcite growth rate and Sr partitioning on solution stoichiometry: non-Kossel crystal growth. Geochimica et Cosmochimica Acta 71, 2240–2249.

Orberger, B., Vymazalova, A., Wagner, C., Fialin, M., Gallien, J.P., Wirth, R., Pasava, J., Montagnac, G., 2007. Biogenic origin of intergrown Mo-sulphide- and carbonaceous matter in lower ambrian black shales (Zunyi Formation, southern China). Chemical Geology 238, 213–231.

Paquette, J., Reeder, R.J., 1995. Relationship between surface structure, growth mechanism, and trace element incorporation in calcite. Geochimica et Cosmochimica Acta 59, 735–749.

Pastero, L., Costa, E., Alessandria, B., Rubbo, M., Aquilino, D., 2003. The competition between {10 14} cleavage and {01 12} steep rhombohedra in gel growth calcite crystals. Journal of Crystal Growth 247, 472–482.

Proux, O., Nassif, V., Prat, A., Ulrich, O., Lahera, E., Biquard, X., Menthonnex, J.J., Hazemann, J.L., 2006. Feedback system of a liquid nitrogen cooled double-crystal monochromator: design and performances. Journal of Synchrotron Radiation 13, 59–68.

Ravel, B., Newville, M., 2005. ATHENA and ARTEMIS: interactive graphical data analysis using IFEFFIT. Journal of Synchrotron Radiation 12, 537–541.

Reeder, R.J., Lamble, G.M., Lee, J.-F., Staudt, W.J., 1994. Mechanism of SeO_4^{2-} substitution in calcite: an XAFS study. Geochimica et Cosmochimica Acta 58, 5639–5646.

Rehr, J.J., Mustre de Leon, J., Zabinsky, S.I., Albers, R.C., 1991. Theoretical X-ray absorption fine structure standards. Journal of the American Chemical Society 113, 5135–5145.

Roman-Ross, G., Cuello, G.J., Turrillas, X., Fernandez-Martinez, A., Charlet, L., 2006. Arsenite sorption and co-precipitation with calcite. Chemical Geology 233, 328–336.

Rouxel, O., Fouquet, Y., Ludden, J.H., 2004. Subsurface processes at the Lucky Strike hydrothermal field, Mid-Atlantic ridge: evidence from sulfur, selenium and iron isotopes. Geochimica et Cosmochimica Acta 10, 2295–2311.

Scheinost, A., Charlet, L., 2008. Selenite reduction by mackinawite, magnetite and siderite: XAS characterization of nanosized redox products. Environmental Science and Technology 42, 1984–1989.

Schmidt, M., Stumpf, T., Marques Fernandes, M., Walther, C., Fanghänel, T., 2008. Charge compensation in solid solutions. Angewandte Chemie International Edition 47, 5846–5850.

Schmidt, M., Stumpf, T., Walther, C., Geckeis, H., Fanghänel, T., 2009. Incorporation versus adsorption: substitution of Ca^{2+} by Eu^{3+} and Cm^{3+} in aragonite and gypsum. Dalton Transactions 33, 6645–6650.

Seifritz, W., 1990. CO_2 disposal by means of silicates. Nature 345, 486.

Sigg, L., Behra, P., Stumm, W., 2000. Chimie des Milieux aquatiaques, 3rd. ed. Dunod, Paris.

Stipp, S.L.S., Christensen, J.T., Lakshtanov, L.Z., Baker, J.A., Waight, T., 2006. Rare Earth element (REE) incorporation in natural calcite: upper limits for actinide uptake in a secondary phase. Radiochimica Acta 94, 523–528.

Stumm, W., Morgan, J.J., 1995. Aquatic Chemistry: Chemical Equilibria and Rates in Natural Waters, 3rd. ed. John Wiley & Sons. (1024 pp.).

Stumpf, T., Marques Fernandes, M., Walther, C., Dordenne, K., Fanghanel, T., 2006. Structural characterization of Am incorporated into calcite: a TRLFS and EXAFS study. Journal of Colloid and Interface Science 302, 240–245.

Tang, Y., Elzinga, E.J., Lee, Y.L., Reeder, R.J., 2007. Coprecipitation of chromate with calcite: batch experiments and X-ray absorption spectroscopy. Geochimica et Cosmochimica Acta 71, 1480–1493.

Temman, M., Paquette, J., Vali, H., 2000. Mn and Zn incorporation into calcite as a function of chloride aqueous concentration. Geochimica et Cosmochimica Acta 64, 2417–2430.

Teng, H.H., Dove, P.M., Orme, C.A., De Yoreo, J.J., 1998. Thermodynamics of calcite growth: baseline for understanding biomineral formation. Science 282, 724–727.

Wen, H.J., Qiu, Y.Z., 2002. Geology and geochemistry of Se-bearing. Formation in Central China. International Geology Review 44, 164–178.

Yudovich, Y.E., Ketris, M.P., 2006. Selenium in coal: a review. International Journal of Coal Geology 67, 112–126.